

Optical Counterparts to X-ray sources in LSST DP1

YUANKUN (DAVID) WANG,¹ ERIC C. BELLM,¹ ROBERT I. HYNES,² YUE ZHAO,³ POSHAK GANDHI,³
LILIANA RIVERA SANDOVAL,⁴ SANDRO CAMPOS,⁵ NEVEN CAPLAR,¹ MELISSA DELUCCHI,⁵ KONSTANTIN MALANCHEV,⁵ AND
TOBIN M. WAINER¹

¹*DIRAC Institute, Department of Astronomy, University of Washington, 3910 15th Avenue NE, Seattle, WA 98195, USA*

²*Department of Physics and Astronomy, Louisiana State University, Baton Rouge, LA 70803-4001, USA*

³*School of Physics & Astronomy, University of Southampton, SO17 1BJ, UK*

⁴*Dept. of Physics and Astronomy, University of Texas Rio Grande Valley, Brownsville, TX 78520, USA*

⁵*The McWilliams Center for Cosmology & Astrophysics, Department of Physics, Carnegie Mellon University, Pittsburgh, PA 15213, USA*

Abstract

We present a crossmatch between a combined catalog of X-ray sources and the Vera C. Rubin Observatory Data Preview 1 (DP1) to identify optical counterparts. The six fields targeted as part of DP1 include the Extended Chandra Deep Field South (E-CDF-S), the Euclid Deep Field South (EDF-S), the Fornax Dwarf Spheroidal Galaxy (Fornax dSph), 47 Tucanae (47 Tuc) and science validation fields with low galactic and ecliptic latitude (SV_95_-25 and SV_38_7, respectively). We find matches to 2314 of 3830 X-ray sources. We also compare our crossmatch to DP1 in the E-CDF-S field to previous efforts to identify optical counterparts. The probability of a chance coincidence match varies across each DP1 field, with overall high reliability in the E-CDF-S field, and lower proportion of high-reliability matches in the other fields. The majority of previously known sources that we detect are, unsurprisingly, active galaxies. We plot the X-ray-to-optical flux ratio against optical magnitude and color in an effort to identify Galactic accreting compact objects using a *Gaia* color threshold transformed to LSST $g-i$, but do not find any strong candidates in these primarily extragalactic counterparts. The DP1 dataset contains high-cadence photometry collected over a number of nights. We calculate the Stetson J variability index for each object under the hypothesis that X-ray counterparts tend to exhibit higher optical variability; however, the evidence is inconclusive whether our sample is more variable over DP1 timescales when compared to field objects.

1. INTRODUCTION

The X-ray sky provides a window into high-energy processes in extreme environments across the universe. X-ray surveys offer an important way to discover a range of interesting and rare objects such as low mass X-ray binaries (LMXBs), binary and isolated millisecond pulsars (MSPs), cataclysmic variables (CVs), as well as other accreting objects like AGN. Over the last 25 years, missions such as *Chandra*, *XMM-Newton*, *Swift*, and *eROSITA* have revealed about a million sources, a small fraction of which have been classified with the aid of multiwavelength observations, while the majority remain unidentified.

Since the localization of X-ray sources is generally less precise than that of optical catalogs, the higher density of the latter often results in multiple optical sources

falling within a single X-ray error circle. As a result, a variety of techniques have been developed to evaluate the strength of each potential match. One common technique is known as the likelihood ratio (LR) method, which estimates the probability that a given counterpart is the true match given the local stellar densities and distribution (Richter 1975; Sutherland & Saunders 1992a). This is among the most widely adopted techniques, such as in the crossmatch between X-ray and optical sources in the ROSAT Bright source catalog and the USNO A-2 optical catalog (Rutledge et al. 2000), or the Chandra Galactic Bulge Survey (Wevers et al. 2016). More recently, Bayesian methods that incorporate priors and probabilities for probabilistic cross-identification have been developed (Budavári & Szalay 2008; Budavári & Basu 2016; Shi et al. 2019) and these methods have been also applied to the ROSAT all sky survey (Haakonsen & Rutledge 2009). Some of these techniques, such as NWAY (Salvato et al. 2018) can evaluating multiple can-

didates or null matches across multiple catalogs jointly. In the past few years, [Bykov et al. \(2022\)](#) used machine learning techniques, training a neural network to perform an optical crossmatch of *eROSITA* sources in the Lockman Hole.

All of these techniques assume knowledge of the photometric priors, which is typically derived from known matched samples. However, the training and validation datasets for these models must be based on unambiguous matches ([Salvato et al. 2018](#)). In addition, many published crossmatches focus on a small area of the sky, such as the Lockman Hole Field, which display advantageous qualities, such as relative uniformity in density and absorption. Additionally, these methods assume that the depth in the X-ray sample used to develop the model is the same as for the X-ray catalog being crossmatched to. Quantities such as X-ray depth and absorption vary across the sky, making a reliable all-sky crossmatch difficult.

Compounding this fact, the upcoming Legacy Survey of Space and Time (LSST) by the Vera C. Rubin Observatory ([Ivezić et al. 2019](#)) will provide the deepest all-sky optical catalog to date. LSST will observe more than 18,000 sq. deg. of the southern sky in six broadband filters (u, g, r, i, z, y) to single-visit depths of 24.5 mag and co-added depths of 27.5 mag. A crossmatch between LSST and the latest X-ray all-sky surveys, such as *eROSITA*, has the potential to uncover vast numbers of rare objects. The high density of optical sources will make building a reliable set of unambiguous matches more difficult than ever. However, with roughly 3-4 days between visits, the cadence of LSST will enable an orthogonal approach towards evaluating potential optical counterparts, as each candidate will include not only color information, but time domain data as well. Many X-ray emitting objects are also transient or variable at optical wavelengths (see table 1) and we thus aim to leverage this fact to aid in the identification of optical counterparts.

To evaluate the difficulty of performing an X-ray/optical crossmatch at LSST depths, as well as the concept of using variability to aid in counterpart identification, we perform a crossmatch between a combined X-ray catalog of sources from several X-ray missions, and the first data preview from Rubin Observatory. The Rubin Observatory Data Preview (DP1; [NSF-DOE Vera C. Rubin Observatory 2025a](#)), released June 30, 2025, is the first on sky “science-grade” dataset and the second of three data previews from LSST. It comprises about 2,000 exposures from seven fields captured with the LSST Commissioning Camera (LSSTComCam) in November and December 2024. DP1 includes raw and

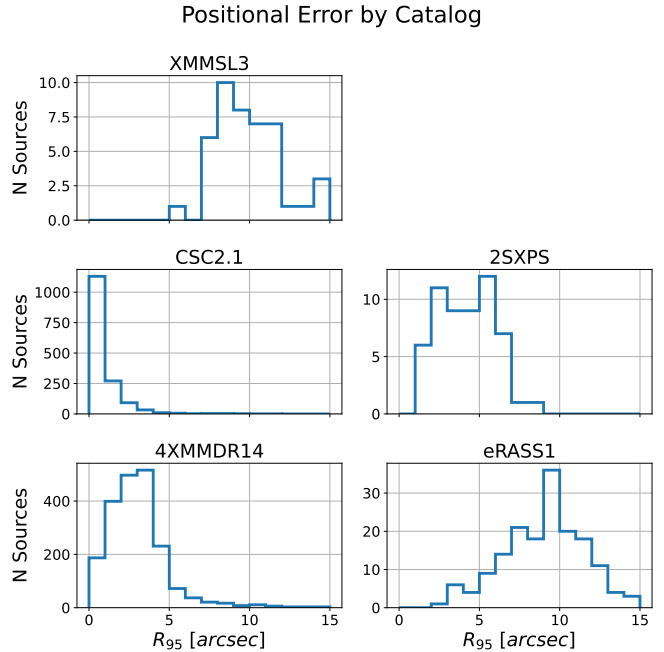


Figure 1. Histogram of R_{95} positional errors of all X-ray sources in DP1 observed fields by catalog.

pipeline-processed visit images, visit-level source catalogs, co-added images with object catalogs, forced source catalogs, difference images and difference image analysis (DIA) catalogs, and other Science Support Products delivered via the Rubin Science Platform for early-science testing. This preview allows the community to validate the pipelines, explore real early data, and prepare for the full LSST survey.

In Section 2, we present the X-ray catalogs we selected and combined, as well as the contents of and data products we utilized in DP1. We also discuss challenges of performing the crossmatch to dense optical fields and how we utilize LSDB ([Caplar et al. 2025](#)) to perform the crossmatch. In Section 3, we present the crossmatched catalog and evaluate the most likely optical counterparts. In Section 4 compare to crossmatches to known sources in the DP1 fields, and examine where the most reliable matches fall in X-ray and optical feature space. In Section 5, we summarize our findings and look ahead to our expectations for LSST.

2. METHODS

2.1. X-ray Catalog

We began by assembling a combined X-ray catalog from the most up-to-date releases for five X-ray catalogs: the *Chandra* source catalog (CSC2.1; [Evans et al. 2024](#)), the *XMM-Newton* serendipitous source catalog (4XXM-DR14; [Webb et al. 2020](#)), the *XMM-Newton* slew survey

Object Type	X-ray Mechanism	Optical Signature	Timescale
Flare Star	Coronal reconnection	Rapid optical flares	Minutes-hours
Active Binary	Coronal reconnection	Ellipsoidal variations, eclipses	Hrs-days
Cataclysmic Variable	White dwarf accretion	Outbursts, eclipses	Hrs-days (outbursts)
X-ray Binary	NS/BH accretion	Ellipsoidal variations, outbursts	Hrs-days (orbital), weeks-months (outbursts)
AGN / Quasar	Accr. Disk corona around SMBH	Aperiodic variability	Days-years
TDE	Stellar disruption by BH	Power-law decay	Days-months

Table 1. Summary of X-ray emitting objects with their optical variability features and timescales.

Catalog	Column	Significance / Range	Notes
CSC2.1	err_ellipse_r0	1.960σ (95%)	Major axis of the error ellipse
	flux_aper90_avg_b	0.5–7.0 keV	Background-subtracted, aperture-corrected, 90% ECF aperture
4XMMDR14	SC_POSERR	0.933σ (63%)	Weighted average of the total POSERR for source
	SC_EP_8_FLUX	0.2–12.0 keV	Mean, error-weighted combined band flux
XMMSL3	radec_err	1σ (68%)	Statistical error on source position from detection software
	flux_b8	0.2–12.0 keV	Total energy band flux
2SXPS	Err90	1.645σ (90%)	90% confidence radial position error on the source position
	PowFlux	0.3–10.0 keV	From power-law indicated by WhichPow
eRASS1	RADEC_ERR	1σ (68%)	Combined positional error, raw output from PSF fitting
	ML_FLUX_P[1..5]	0.2–8.0 keV	Sum of bands 1–5 where $\text{DET_LIKE_P}[\text{band}] \geq 7$

Table 2. Positional uncertainty and flux column details for each X-ray catalog.

catalog (XMMSL3; Saxton et al. 2008), the Swift-XRT point source catalog (2SXPS; Evans et al. 2020), and the *eROSITA* all-sky survey source catalog (eRASS1; Merloni et al. 2024). From each catalog, we selected the extract the name, right ascension, declination, positional uncertainty, and broadband X-ray flux.

The column names for the broadband flux and positional uncertainty are listed in Table 2. In each case we choose the column that accounts for both systematic uncertainty and positional uncertainty from source detections. For *Chandra*, we take the major axis of the error ellipse as our uncertainty radius. We take this uncertainty and scale it to a 1σ error radius $R_{1\sigma}$. Then, assuming Gaussian errors, we multiply to get the 95% error radius $R_{95} = 1.96R_{1\sigma}$.

Since the energy range of the broadband flux is different for each instrument, we list the energies in Table 2, as well as an additional description of the flux pulled from the documentation for each catalog. The eRASS1 broadband flux was calculated by adding bands 1 to 5 for each X-ray source, provided the source is detected with $\text{DET_LIKE_P}[\text{band}] \geq 7$, for a moderate strength detection in that band. The distribution of positional errors in each catalog are plotted in Figure 1.

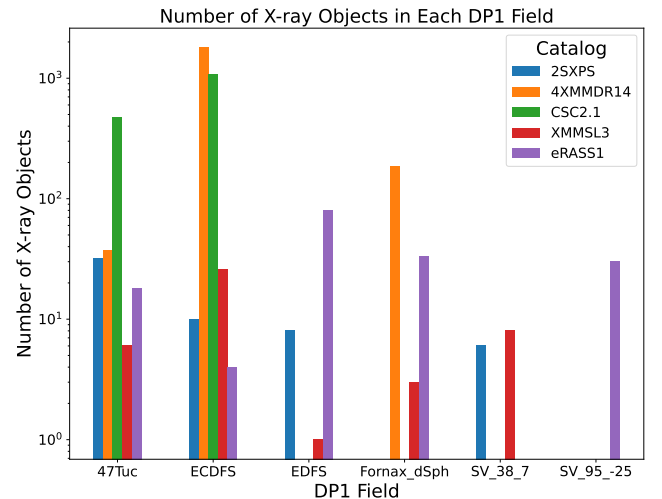


Figure 2. Number of X-ray sources by X-ray catalog in each DP1 field. The majority of X-ray sources are found in the Extended Chandra Deep Field - South (E-CDF-S), which is well observed by X-ray telescopes.

We then performed a 1.5 degree conesearch around the center of each of the 6 DP1 fields we include in our crossmatch to isolate only the X-ray sources near these fields, yielding 10,307 sources. We then de-duplicated the catalogs by crossmatching between all pairs of X-

ray catalogs to get all sources that fall within the 95% error circle for another source. For 1:1 matches, we assume the two sources are the same and keep the source with the smaller positional uncertainty. For sources with multiple matches, we keep only the sources from the catalog with the smaller positional uncertainty. This leaves 9248 sources. We finally impose a $15''$ limit on the 95% error radius, which eliminates outliers and leaves 9089 total sources. Finally, to eliminate all sources that are never observed as part of DP1, we find the tract and patch of each position using the DP1 `skymap`, leaving a total of 4481 final sources in our X-ray catalog. The number of X-ray sources in each DP1 field, broken out by X-ray survey, is given in Figure 2.

2.2. Optical Catalog

The LSST Data Preview 1 (DP1) contains the first data collected by the Vera C. Rubin Observatory and offers the first look at the characteristics and capabilities of the data that will eventually be in LSST. The dataset consists of images taken by LSSTComCam between November 9 and December 12, 2024 and covers an area of approximately 15 sq. deg. We selected six of the fields observed by DP1: 47 Tucanae (47 Tuc), the Extended Chandra Deep Field South (E-CDF-S), the Euclid Deep Field (EDF-S), the Fornax Dwarf Spheroidal Galaxy (Fornax dSph), and two science validation fields, one at low galactic latitude (SV_95_-25) and one at low ecliptic latitude (SV_37_7) (NSF-DOE Vera C. Rubin Observatory 2025a), excluding the Seagull Nebula field which contains extensive nebulosity. These fields were observed repeatedly in the *ugrizy* bands over several nights. Observations were made in observing epochs on a given target field, with 5–20 visits in each of three loaded filters at a time. Each visit consists of one 30 second exposure covering approximately half a square degree.

The spatial distribution and coverage of the DP1 fields, and the temporal distribution of observations by field and filter can be found in the DP1 science paper (NSF-DOE Vera C. Rubin Observatory 2025a, figures 4-6). The number of visits per field by filter is given in Table 3. The cumulative imaging depth at $S/N = 5$ expressed as a limiting magnitude in each field exceeds 26th in the most observed regions in each field and is visualized in figure 3 of the *Rubin Observatory Plans for an Early Science Program* document (Guy et al. 2025).

For DP1 data, we adopt the Rubin convention of referring to a single-epoch detections within science images as a `Source` and the astrophysical object associated with a given detection as an `Object`. To draw this distinction, we refer to Rubin data products such as `Sources`

and `Objects` in teletype for the remainder of the paper. In other words, every `Object` will usually have multiple associated `Sources`, with each `Source` corresponding to an observation in one single-epoch science image, also known as a `visit_image`. DP1 consists of five types of data products, which are described in detail in NSF-DOE Vera C. Rubin Observatory (2025a): images, catalogs, maps, metadata, and ancillary data products. We utilize the `Object` catalog (NSF-DOE Vera C. Rubin Observatory 2025b), which contains 2,299,726 `Objects`—detections on `deep_coadd` images (NSF-DOE Vera C. Rubin Observatory 2025c) made by stacking all available `visit_images` NSF-DOE Vera C. Rubin Observatory (2025d). To produce lightcurves and calculate time-series features, we require per-visit photometry. We use the `ForcedSource` catalog (NSF-DOE Vera C. Rubin Observatory 2025e), which contains forced photometry at the position of detected `Objects` in each `visit_image`.

The Rubin difference image analysis (DIA) pipeline also detects sources in `difference_images` (NSF-DOE Vera C. Rubin Observatory 2025f), known as `DiaSources` (NSF-DOE Vera C. Rubin Observatory 2025g). By associating `DiaSources` at the same position, the DIA pipeline also builds `DiaObject` catalogs. We also crossmatch to this catalog, which contains 1,089,818 `DiaObjects` (NSF-DOE Vera C. Rubin Observatory 2025h). The DIA pipeline bypasses the deblending step that fails in the densest crowded fields (Choi et al. 2025), such as inner regions of the 47 Tuc and Fornax dSph fields. Other studies have shown that matching to the `DiaObject` table can recover photometry from some of the denser fields (Wainer et al. 2025). More discussion of the `DiaObject` catalog match is found in 4.4.

2.3. Crossmatch to Object table

LSDB was developed by the LSST Interdisciplinary Network for Collaboration and Computing (LINCC) Frameworks project to enable scalable analysis of large catalogs (Caplar et al. 2025). We use the LSDB Hierarchical Adaptive Tiling Scheme (HATS) formatted DP1 `Object` catalog (Malanchev et al. 2025) and the LSDB crossmatch function to crossmatch the combined X-ray catalog to all `Objects` detected in the six DP1 fields. We set the match radius to $15''$ and return up to the 10 closest matches for each X-ray source. We then eliminate all matches where the candidate optical counterpart does not fall within the 95% error radius of the X-ray source. We are left with 4513 candidate `Object` counterparts for 2314 unique X-ray sources.

Since we had narrowed down our catalog of X-ray sources by keeping all sources in tracts and patches ob-

Target	u	g	r	i	z	y
47 Tuc	6	10	33	19	0	5
Rubin SV 38 7	0	44	55	57	27	0
Fornax dSph	0	5	26	13	0	0
E-CDF-S	53	230	257	177	177	30
EDF-S	20	61	90	42	42	20
Rubin SV 95 -25	33	86	97	29	60	11

Table 3. Number of visits by field for DP1.

served by LSSTComCam, some of these sources are just past the outskirts of the DP1 fields and are not in the observed footprint. To further eliminate these sources, we find the convex hull of all matches in a field. We then assume that sources interior to the convex hull were observed as a part of DP1 and are therefore optical nondetections. This eliminates 651 of the X-ray sources and leaves us with a final total of 3830 X-ray sources in the footprint of DP1.

Lastly, we repeat the crossmatching, adding $30''$ to the declination of each X-ray source to obtain a random set of matched `Objects`, so we can compare our matches to a control sample of field objects.

2.4. Evaluation of crossmatch reliability

We calculate the reliability¹, which we define as the probability of finding no chance object closer to the X-ray source than the counterpart `Object` (Sutherland & Saunders 1992b). The expected number of background sources within the separation between the source and counterpart is:

$$Y = \pi d^2 \cdot N, \quad (1)$$

where item Y is the expected number of background sources, d is the separation between the source and counterpart, and N is the local background source density (Sutherland & Saunders 1992b). We calculate the background by counting the number of `Objects` in an annulus with an inner radius of the 4σ X-ray error circle, $R_{4\sigma}$, and outer radius of $R_{8\sigma}$ around each counterpart. We obtained these radii by scaling up the $R_{1\sigma}$ calculated in Section 2.1. We set the inner radius to $R_{4\sigma}$ in order not to bias the number density by including the real counterpart. If there are no `Objects` in the annulus, we increase the outer radius by $10''$ until we have at

¹ The crossmatch reliability should not be confused with the Rubin-reported reliability score for `DiaSources`, which is a machine-learned probability that a given `DiaSource` is astrophysical in origin.

least one. Assuming Poisson statistics, the reliability of the match is given by

$$\text{Reliability} = \Pr(0, Y) = e^{-Y}. \quad (2)$$

2.5. Quantifying variability

We also calculate the Stetson J index to quantify the variability of each potential counterpart (Stetson 1996). Let the standardized residual for observation i be defined as

$$\delta_i = \sqrt{\frac{n}{n-1}} \cdot \frac{\nu_i - \bar{\nu}}{\sigma_i}, \quad (3)$$

where ν_i is the observed value (e.g., flux or magnitude), $\bar{\nu}$ is the weighted mean value, σ_i is the uncertainty in ν_i , and n is the total number of observations in the band. Since each LSSTComCam epoch consists of a single observation, we define the product P_i

$$P_i = \delta_i^2 - 1. \quad (4)$$

The Stetson J index is then defined as

$$J = \frac{1}{N} \sum_{i=1}^N \text{sgn}(P_i) \cdot \sqrt{|P_i|}. \quad (5)$$

We calculate the Stetson J index in each band using the `psfFlux` and `psfFluxErr` columns from the forced source table for each `Objects`.

2.6. Value added crossmatches to SIMBAD, Milliquas, Gaia

After we obtained the crossmatch between DP1 `Objects` and our X-ray catalog, we also matched these `Objects` to several other catalogs to provide additional context to our matches and to build up a value-added catalog. We used LSDB to find all Gaia DR3 sources (Gaia Collaboration et al. 2023), within $0.5''$ of the LSST DP1 objects. Since Gaia provides parallaxes and distances, we can use the data to distinguish between Galactic and extragalactic objects for some of the brighter `Objects`. We also find all DP1 sources within $2''$ of any Gaia source brighter than 15th magnitude—these `Objects` are flagged because they may either be saturated, or have inconsistent photometry due to the nearby presence of a bright star.

We also crossmatched the positions of the optical LSST DP1 objects to the Million Quasar (Milliquas) catalog (Flesch 2023), using radius of $1''$ since most of the objects in the catalog are sourced from optical surveys with high precision, such as Gaia eDR3, DESI, and SDSS-DR18. We expect many of our matches in the E-CDF-S and EDF-S fields, which are away from the

galactic plane, to be extragalactic, and this crossmatch will enable us to compare the properties of known active galaxies to our broader set of matches.

Lastly, we used astroquery (Ginsburg et al. 2019) to query any existing object type (otype) from SIMBAD (Wenger et al. 2000) within $1''$ of the position of the `Object` location, and any associated photometry in the *ugri* and *V* bands. We then drop duplicate matches such that all remaining matches are between one SIMBAD source and one DP1 `Object`.

3. RESULTS

3.1. Crossmatch results

A total of 4513 candidate `Objects` are found within the 95% error radius for 2314 unique X-ray sources, as some X-ray sources have multiple DP1 `Objects` within the R_{95} . Figure 3 shows the locations of all objects in the original combined X-ray catalog from Section 2.1 that were observed in the DP1 fields, as well as whether a counterpart was identified in DP1. 1600 X-ray sources did not have a counterpart in the DP1 `Objects` table. Many of the unmatched X-ray sources lie in the cores of 47 Tuc (466/567) or the Fornax dSph galaxy (129/220), where the LSST pipeline performance is reduced due to the high stellar density and there are no `Objects` detected. Additionally, 669 out of 2910 sources in the E-CDF-S field have no match in our crossmatched dataset. We find matches for all X-ray sources in the EDF-S field, the low galactic latitude science validation field (SV_95_-25), and the low ecliptic latitude field.

The magnitude distribution of the counterparts in each field can be seen in Figure 4. Taking fiducial limiting magnitudes of 21, 23, and 24 for Gaia (Gaia Collaboration et al. 2023), SDSS (York et al. 2000), and PanSTARRS (Kaiser 2004), we find that 78%, 45%, and 27% of DP1 objects were fainter than these surveys, respectively, in all bands. This indicates that during the full survey, we should expect to vastly increase the number of X-ray counterparts.

The total numbers of matches broken out by field and instrument are given in Table 3. We also present the number of matches to external catalogs: Milliquas, Gaia, and SIMBAD, by field. We find a total of 444 matches between our DP1 `Objects` and the Milliquas catalog, 345 between our DP1 `Objects` and Gaia DR3, and 1046 unique matches between our DP1 `Objects` and SIMBAD. We present the code used to generate these online ², removing the DP1 positional and photometry

data to comply with the LSST data rights policy (Blum & the Rubin Operations Team 2020).

3.2. Reliability of crossmatch

Next, we look at the reliability of crossmatch for the most likely counterpart for each unique X-ray source. The reliability is influenced both by the radius of separation between the X-ray source and DP1 match and the local density. As expected, the fields with the most constrained X-ray observations - those made by *Chandra* and *XMM-Newton* - have the highest proportion of high reliability matches.

Figure 5 plots the distribution of reliability in each field. We define a match where the probability of a chance association is less than 10%, i.e. the reliability $\geq 90\%$ to be a high-reliability match and we create a subset of 1344 matches meeting this criteria. The E-CDF-S field has the highest proportion of reliable matches, with a total of 1295, or 60.6% of all matches in that field. On the other hand, the proportion of reliable matches is much lower in the EDF-S and the two science validation fields at between 21% and 25%.

The calculation of the reliability depends on an accurate measurement of the background source number density. This in turn assumes that the `Object` catalog has high completeness—otherwise the density will be underestimated and the reliability will be falsely high. Because we know that the two crowded fields 47 Tuc and Fornax dSph may not meet this requirement, we should treat the reliabilities calculated in these fields with caution.

4. DISCUSSION

4.1. Comparison to E-CDF-S crossmatch in Luo et al. (2017)

Out of 1055 total objects in the E-CDF-S X-ray catalog in Luo et al. (2017), we find 777 counterparts in the `Object` catalog within the 2σ error radius and 900 counterparts in the 3σ error radius. Of the remaining 155 *Chandra* sources, 79 are only detected in bands with wavelength longer than LSST y-band, or have no optical or IR counterpart in the original study either. The final 75 sources with Hubble Space Telescope (HST) counterparts in either R or z band only contains 21 sources brighter than 24th magnitude. We also have one match (LSST-DP1-0-611255759837095315) to one of the 16 X-ray sources with no match in the original paper (No 896). We find that $\log(F_X/F_{r-psfFlux}) = -0.84 > -1$, and the DP1 `refExtendedness` parameter for this `Object` is 1, i.e. extended, which satisfies two of the criteria in the paper for an active galactic nucleus (AGN) classification.

² https://github.com/ykwang1/DP1_Xray_public/

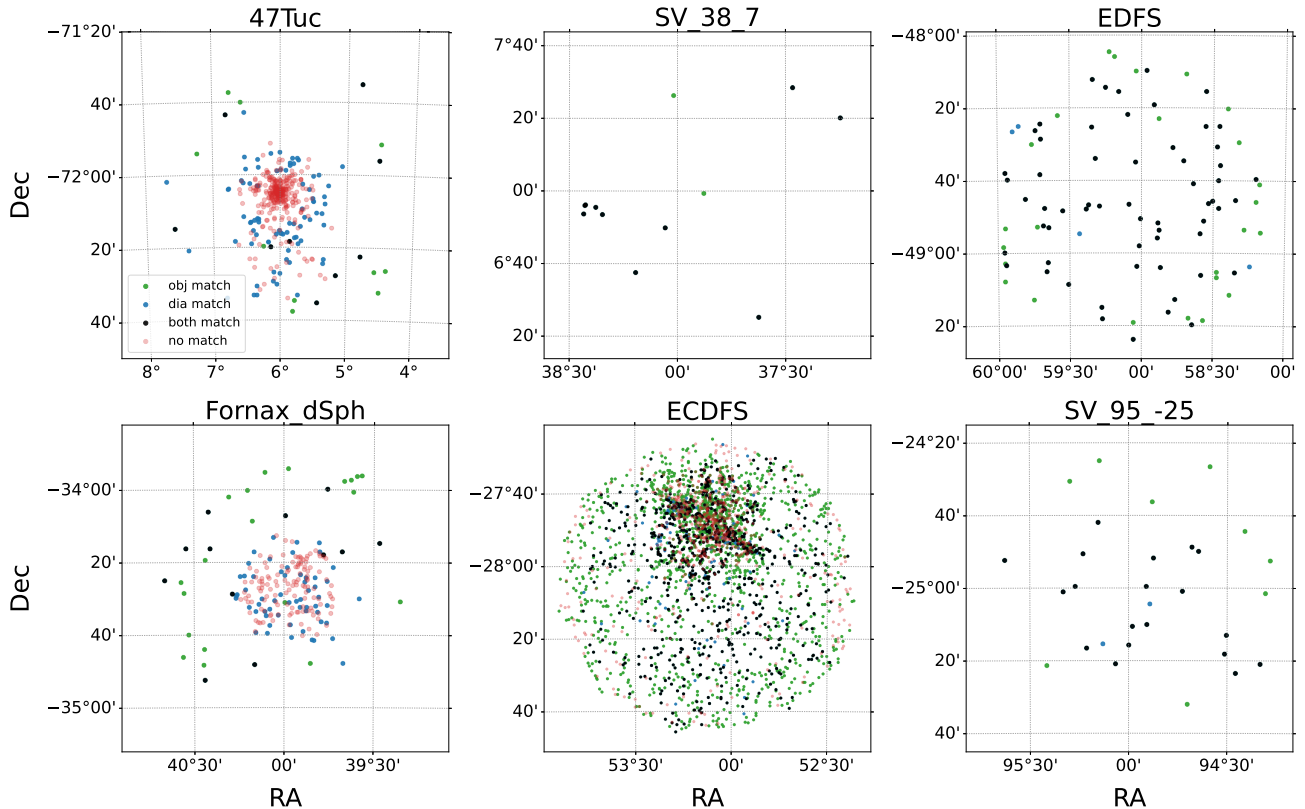


Figure 3. Spatial distribution of all X-ray sources in the combined X-ray catalog. Matches to `Objects` are colored green. We also crossmatched `diaObjects`, which are detections based on `difference_images`. X-ray sources only detected in the `DiaObject` catalog are plotted in blue and sources found in both catalogs are plotted in black. X-ray sources with no optical match in DP1 are plotted in red. Due to the crowdedness of the 47 Tuc and Fornax dSph fields, we have better success matching to the `DiaObject` table (see Section 4.4). Many of the unmatched sources are also in the cores of these two fields for the same reason.

4.2. Variability

We also examine whether the Stetson J index has any relation to the reliability of the closest `Object` counterpart, to test our hypothesis that the optical counterparts to X-ray sources will tend to be more variable. As an example, we plot the lightcurve of high-reliability match with the largest r -band Stetson J in Figure 6. This turns out to be the SU UMa type cataclysmic variable CRTS J033349.8-282244 (Drake et al. 2014; Kato et al. 2017), which completed a full outburst cycle during commissioning observations, and was also found by Malanchev et al. (2025) in their variability search.

Plotting the reliability of crossmatch against the Stetson J index in Figure 7, we find that there appears to be no association between these two metrics. Instead, as seen in the figure, our Stetson J appears more correlated with the magnitude of the `Object`. We perform a 2-sample KS-test with the null hypothesis that the distribution of Stetson J for field stars is the same or greater than as the distribution of Stetson J for our

matches. Due to the magnitude dependence of the Stetson J , we perform this test on samples for matches and field objects of magnitude 17 to 25 in bins of width 2 magnitudes. We also split the samples into $ugri$ bands, for a total of 12 tests. We set our overall threshold $\alpha = 0.05$ for rejecting the null hypothesis and apply the Bonferroni Correction to obtain a per-test threshold of $\alpha/m = 0.0042$, where m is the number of hypotheses. We find that since we reject the null hypothesis for only two of these subsets at the $p < 0.0042$ level, so we have at best weak evidence that the matches are more variable than the field objects.

The dense cadence of the commissioning observations means the Stetson J s are most sensitive to variability on timescales of seconds to days, since the majority of the DP1 observations will be on these timescales. This differs from much of the expected longer variability timescales of most X-ray counterparts, particularly AGN, which we expect to make up the vast majority of our counterparts. However, the upcoming LSST full survey will probe nearly the full range of variability

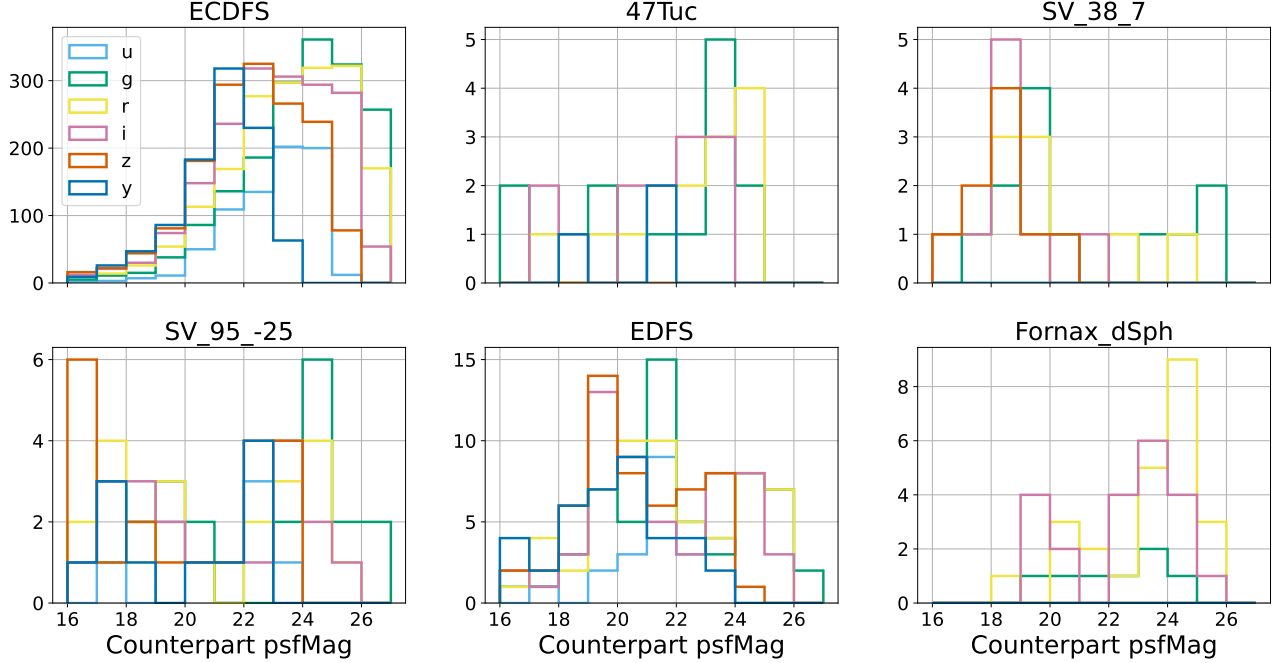


Figure 4. The magnitude distribution of the counts of candidate counterparts in each of the 6 fields, by band. Many of the crossmatched counterparts are fainter than the Gaia, PanSTARRS and SDSS limiting magnitudes. Only measurements where the $\text{SNR} \geq 5$, where $\text{SNR} = \text{psfFlux}/\text{psfFluxErr}$ are in the histograms.

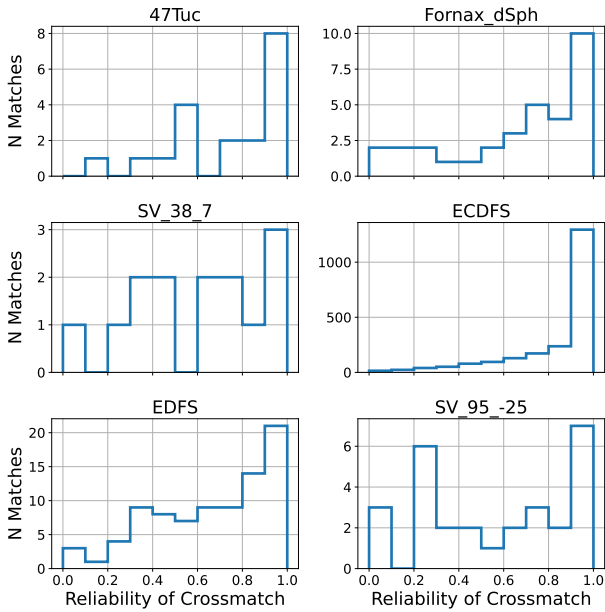


Figure 5. The reliability of crossmatch of the closest counterpart to each X-ray source, broken out by field. The reliability is the probability the counterpart is not a random association.

timescales, and so similar analyses may be more informative in the future.

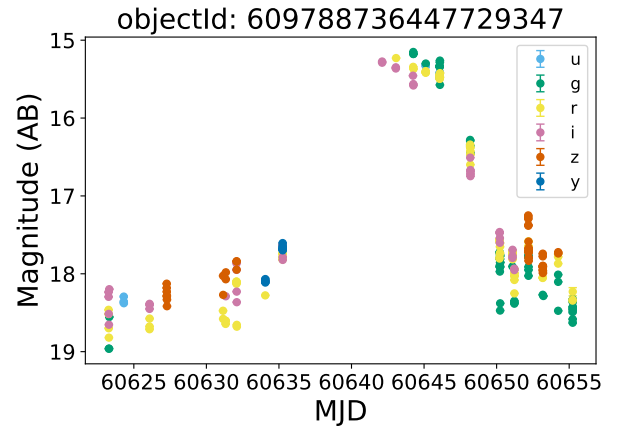


Figure 6. An example lightcurve of one of our counterparts, the SU UMa type cataclysmic variable CRTS J033349.8-282244, which was observed in outburst. This Object had the highest r -band Stetson J out of all of our high-reliability matches.

4.3. Plots in optical-X-ray parameter space

A full classification of all the X-ray sources with DP1 counterparts is beyond the scope of this paper. However, we take advantage of our crossmatch to the Milliwas catalog and our SIMBAD queries to show where a sample of objects of known object type lie in our optical-

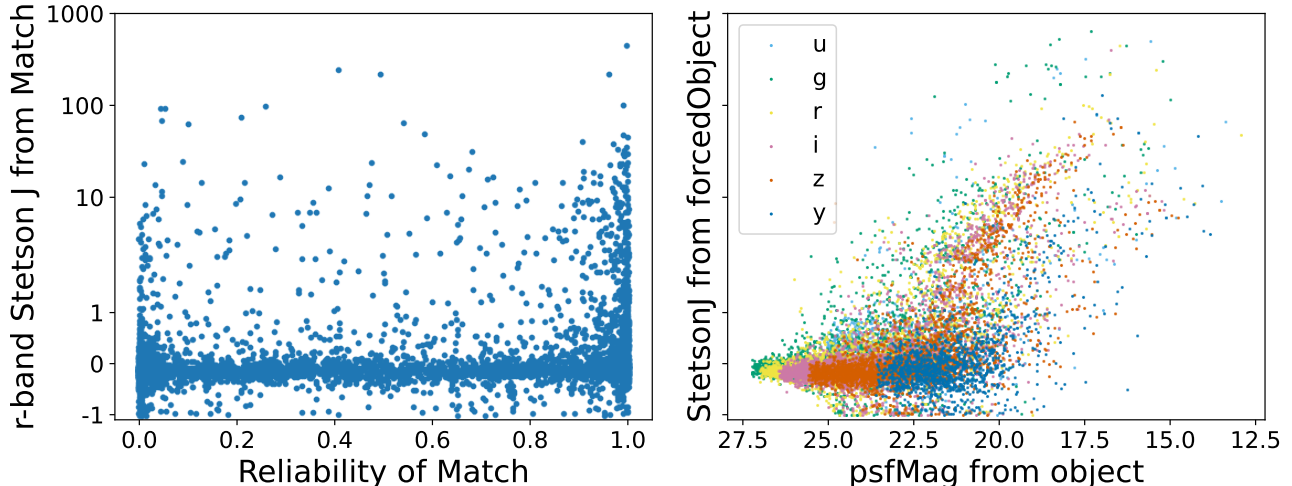


Figure 7. There is no apparent association between the reliability of a crossmatch and the Stetson J index of the object. Conversely, the Stetson J appears to be systematically higher for brighter Objects. We use a symmetric logarithmic (symlog) scale for the y-axis.

X-ray parameter space. In Figure 8, we make two sets of two plots each. On the left, we plot “control samples” of classified objects. On the right, we plot all matched DP1 Objects that have a reliability greater than 90%.

The top left subplot shows our 444 Object sample of matches to the Milliquas catalog in the i-magnitude / X-ray broadband flux plane, similar to figure 3 in Hasinger (2008). Our results are consistent, with most sources falling between the lines of constant X-ray to optical flux ratio of $\log(F_X/F_{opt}) \pm 1$. For sources with fluxes between 10^{-14} and 10^{-12} ergs $^{-1}$ cm $^{-2}$. Below 10^{-14} ergs $^{-1}$ cm $^{-2}$ it appears some of the AGN in our sample have smaller $\log(F_X/F_{opt})$. We also see much more scatter in the top right plot, even though we expect most of the sources to be extragalactic as well.

The bottom left subplot shows the log flux ratio $\log(F_X/F_{opt})$ against the color. We choose to plot $g - i$ color, and plot the empirical cut from Rodriguez (2024) onto our subplot using the following transformation:

$$y = -0.079 + 1.184x + 0.2218x^2 - 0.1013x^3 \quad (6)$$

Where y is LSST $g - i$ color and x is Gaia $BP - RP$, for x between approximately -1 and 2 (Gwyn 2024). This cut and diagram, termed the X-ray Main Sequence, is a useful tool for separating Galactic X-ray sources into stellar and compact object regions. Although the vast majority of our sources are extragalactic, we plot our Milliquas matches plus a handful of known Galactic stars and one cataclysmic variable (CRTS J033349.8-282244). We note that this CV was actually in outburst (see Figure 6), and we calculate the optical flux and color in quiescence by selecting the forced photometry before

and after the outburst. The known stars fall on the opposite side of the cut as the CV. We also see that the quasi-stellar objects (QSOs) are much bluer and have a higher flux ratio than the AGN.

On the bottom right, we again plot the matched DP1 Objects that have a reliability greater than 90% in the same parameter space. On color, we have the `refExtendedness`, a measure of whether the DP1 Object is point-like (0) or extended (1). These classifications are roughly meant to correspond to star-like and galactic sources. However, from our sample of known sources, we find that this is not always dependable, as QSOs are classified as point-like about 1/3 of the time (77/221). We also notice that our CV is classified as an “extended” source as well. For future followup, we would begin by selecting the set of sources in the upper right of the plot with point-like `refExtendedness` and in fields other than E-CDF-S and EDF-S for investigation as potential accreting systems.

4.4. *difference_images* and crossmatch to the *DiaObject* catalog

DP1 also contains catalogs of detections by the Difference Image Analysis pipeline (DIA) in the `difference_images`. Detections on individual `difference_images` are known as `DiaSources` and the difference image analysis pipeline associates `DiaSources` together to create a catalog of `DiaObjects`, the equivalent to the `Object` table for difference image analysis. We expect transients and variables to show up in the `DiaObject` catalog and thus this is another way to assess whether an Object is variable. Simi-

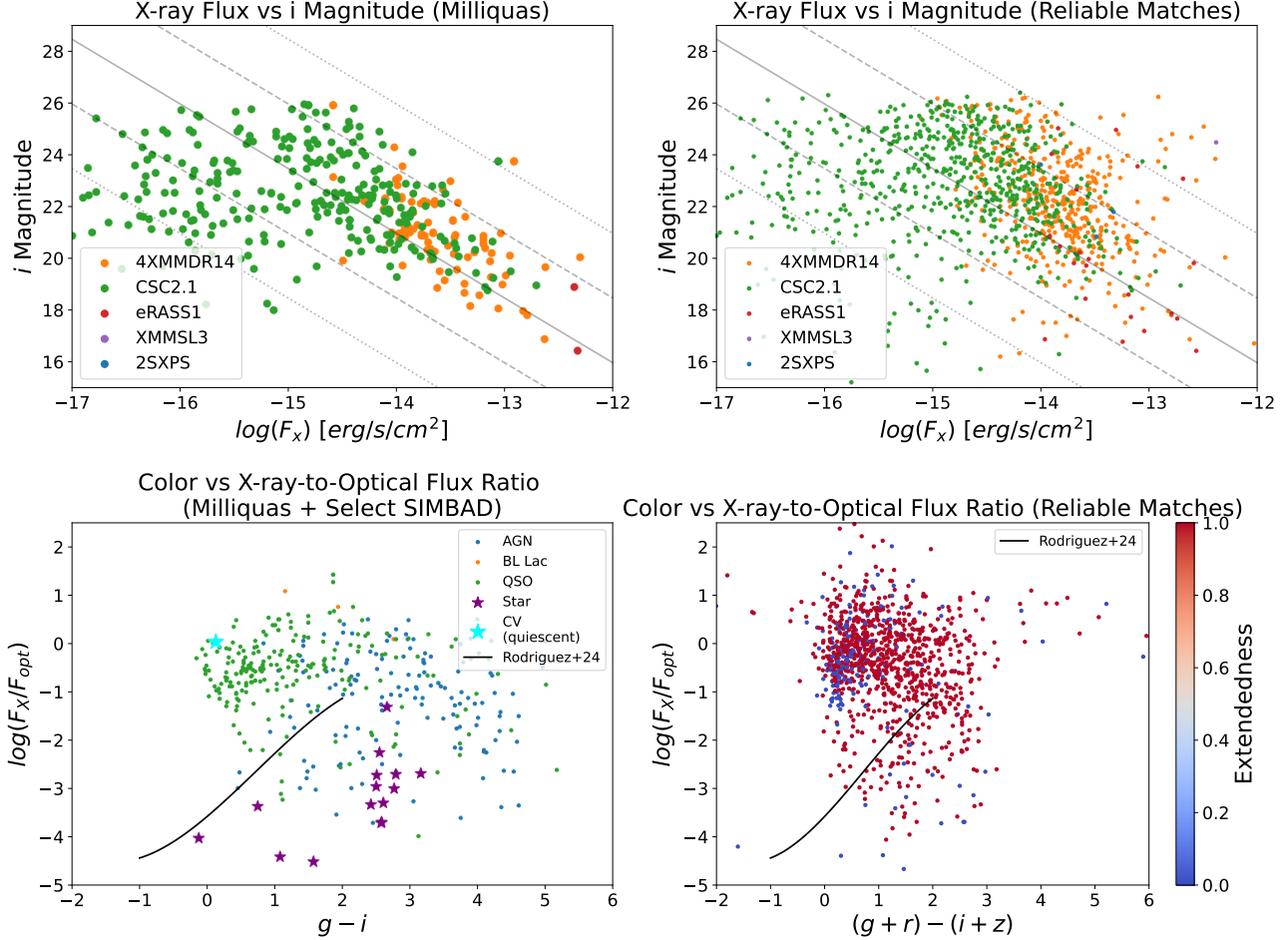


Figure 8. TOP: On the left, we plot the X-ray flux vs i-band magnitude, only for objects with matches to the Milliquas catalog. The solid grey line delineates $\log(F_x/F_{opt}) = 0$, and the dashed and dotted lines are at log flux ratios of ± 1 and ± 2 respectively. Most of the X-ray bright galaxies fall between ± 1 , as expected for AGN. The right plot shows all matches with reliability $> 90\%$, a total of 1344 objects, on the same axes. BOTTOM: We plot the X-ray-to-optical flux ratio against color. The left plot contains matches to Milliquas, plus some stars from SIMBAD and Gaia, and one CV (CRTS J033349.8-282244). The right plot again shows all matches with reliability $> 90\%$ on the same axes. Extendedness measures whether the matched DP1 object is point-like (0) or extended (1). We use color transformations as defined in our Equation 6 to plot the empirical cut from Rodriguez (2024).

lar to the `ForcedSource` catalog, DP1 also includes a `ForcedSourceOnDiaObject` (NSF-DOE Vera C. Rubin Observatory 2025i) catalog containing forced photometry on the `visit_images` at the location of each `DiaObject`. Additionally, the `DiaSource` catalog contains all photometry of each `DiaSource` that is associated with a given `DiaObject`.

We crossmatch the locations of all the X-ray sources to the `DiaObject` catalog and find 2276 candidate `DiaObjects` for 1067 unique X-ray sources. 815 X-ray sources have counterparts in both the `Object` and `DiaObject` catalogs, although we cannot confirm that the `DiaObject` and `Object` are the same astronomical object for all 815 sources. Thus, of the 3830 X-ray

sources in the combined X-ray catalog, 2566 have at least one match between the `Object` and `DiaObject` tables. We note that many X-ray sources in the 47 Tuc and Fornax dSph fields only have matches to the `DiaObject` catalog.

Since there is no `difference_image` equivalent to a co-added image, we calculate the error-weighted mean magnitude in each band of every `DiaObject` using the `psfMag` and `psfMagErr` columns in the `ForcedSourceOnDiaObject` table as the per-band photometry of each `DiaObject`.

5. CONCLUSIONS

We performed a crossmatch between a consolidated catalog of all objects in the DP1 fields in five X-ray cat-

Feature	Subset	Field						Total
		47 Tuc	E-CDF-S	EDF-S	Fornax_dSph	SV_38_7	SV_95_-25	
X-ray sources with Object match	2SXPS	0	8	8	0	6	0	22
	4XMMDR14	4	1279	0	2	0	0	1285
	CSC2.1	3	821	0	0	0	0	824
	XMMSL3	2	24	1	3	8	0	38
	eRASS1	10	4	76	27	0	28	145
	Total	19	2136	85	32	14	28	2314
X-ray sources with DiaObject match	...	91	810	64	71	10	21	1067
Any Object or DiaObject match	...	101	2241	89	91	14	30	2566
No Object or DiaObject match	...	466	669	0	129	0	0	1264
N_{Object} in R_{95}	...	75	3560	429	195	57	197	4513
$N_{\text{DiaObject}}$ in R_{95}	...	249	1587	176	106	31	127	2276
Crossmatch Reliability	> 90%	8	1295	21	10	3	7	1344
refExtendndess	point-like (0)	7	379	23	14	1	8	432
	extended (1)	7	1617	53	16	10	11	1714
	unknown (NA)	5	140	9	2	3	9	168
External xmatches	Gaia	10	235	45	19	8	28	345
	Milliquas	2	434	3	0	5	0	444
	SIMBAD	1	1036	2	1	2	4	1046

Table 4. Breakdown of matches by field. The first section details the number of X-ray sources with DP1 **Object** matches for each catalog, as well as the sources with matches to **DiaObjects**, detections on **difference_images**. Since some sources are only detected in either the **deep_coadds** or **difference_images**, as seen in Figure 3, we also present numbers of X-ray sources with any **Object** or **DiaObject** match, as well as those with no match. The second section gives the total numbers of **Objects** and **DiaObjects** found in the 95% error radius of any X-ray source—some sources having multiple matches. We also show the number of high reliability matches (> 90%), the number of point-like vs. extended **Objects**, and the number of **Objects** with matches to external catalogs

alogs to `DP1 Objects` and `diaObjects`. Our results demonstrate that we are able to find many candidate counterparts with high reliability. Many of the candidate counterparts are fainter than Gaia, PanSTARRs, and SDSS limiting magnitudes. We find that 2566 out of 3830, or roughly 67% of our X-ray sources have a match in one of the DP1 catalogs. After examining the X-ray to optical flux ratios of these matches, we do not follow up any of these sources at the present. A list of X-ray sources with optical non-detections, which may also be of interest for future followup, can be found in the linked GitHub.

Many previous studies with deeper X-ray to optical crossmatches focus on a specific field such as E-CDF-S (Luo et al. 2017), the Lockman Hole (Salvato et al. 2018; Bykov et al. 2022), or the galactic bulge (Wevers et al. 2016). The LSST DP1 dataset contains six fields with very different density, observing depth, and coverage by X-ray catalogs, and we attempted to apply the same crossmatching procedure to each field. We find that many of our crossmatches are reliable in fields that are well observed by X-ray missions, i.e. the E-CDF-S field. In the non-crowded fields where we expect the completeness of the `Object` catalog to be high, we find that at least 20% of our matches are reliable. In the crowded fields 47 Tuc and Fornax dSph, the majority of matches are found only on `diaObjects`, which bypass the deblending on co-add image step of the pipeline. We expect that it will be feasible to build up the large datasets of reliable optical-X-ray matches across the LSST all-sky survey to extract the local magnitude and sky density by magnitude distributions needed to implement and train more sophisticated crossmatching models, but that this will require much larger survey area than the current DP1 fields.

The variability quantified by the Stetson J index does not appear to correlate with the reliability of the crossmatch, and it remains inconclusive whether increased optical variability can indicate a higher likelihood counterpart, despite our prior that should be the case. As the Rubin Science Pipelines continue to be developed, we will check back to see if this effect persists. Additionally, the continuous cadence of the commissioning observations mean the Stetson J s are most sensitive to variability on timescales of seconds to days, since the DP1 observations were on these timescales. This differs from much of the expected longer variability timescales of most extragalactic X-ray counterparts. However, the upcoming LSST full survey will probe nearly the full range of variability timescales and we plan to redo this analysis in the future once the survey is well underway.

Overall, while challenges remain, the DP1 data shows promise for X-ray optical association. Continued improvements to the Rubin Science Pipelines and in-kind programs, particularly those dedicated to crowded-field stellar photometry, are expected to deliver even better results in future data previews and data releases. These broader datasets should permit the utilization of more advanced statistical and machine learning based crossmatching techniques that can that will enable comprehensive classifications of X-ray sources and searches for rare and exotic new objects.

ACKNOWLEDGMENTS

YDW and ECB acknowledge support from the Vera C. Rubin Observatory, which is supported in part by the National Science Foundation through Cooperative Agreements AST-1258333 and AST-2241526 and Cooperative Support Agreements AST-1202910 and 2211468 managed by the Association of Universities for Research in Astronomy (AURA), and the Department of Energy under Contract No. DE-AC02-76SF00515 with the SLAC National Accelerator Laboratory managed by Stanford University. Additional Rubin Observatory funding comes from private donations, grants to universities, and in-kind support from LSST-DA Institutional Members.

YDW and ECB acknowledge support from the DiRAC Institute in the Department of Astronomy at the University of Washington. The DiRAC Institute is supported through generous gifts from the Charles and Lisa Simonyi Fund for Arts and Sciences, Janet and Lloyd Frink, and the Washington Research Foundation.

Support was provided by Schmidt Sciences, LLC. for S. Campos, N. Caplar, and K. Malanchev.

This research has made use of data obtained from the *XMM-Newton* survey source catalogue compiled by the *XMM-Newton* Survey Science Centre consortium in collaboration with members of the *XMM-Newton* SOC and the EPIC consortium.

This research has made use of data obtained from the 4XMM *XMM-Newton* serendipitous source catalogue compiled by the *XMM-Newton* Survey Science Centre consortium.

This research has made use of data obtained from the Chandra Source Catalog, provided by the Chandra X-ray Center (CXC).

This work made use of data supplied by the UK *Swift* Science Data Centre at the University of Leicester.

This work is based on data from *eROSITA*, the soft X-ray instrument aboard SRG, a joint Russian-German science mission supported by the Russian Space Agency

(Roskosmos), in the interests of the Russian Academy of Sciences represented by its Space Research Institute (IKI), and the Deutsches Zentrum für Luft- und Raumfahrt (DLR). The SRG spacecraft was built by Lavochkin Association (NPOL) and its subcontractors, and is operated by NPOL with support from the Max Planck Institute for Extraterrestrial Physics (MPE). The development and construction of the *eROSITA*-ray instrument was led by MPE, with contributions from the Dr. Karl Remeis Observatory Bamberg & ECAP (FAU Erlangen-Nuernberg), the University of Hamburg Observatory, the Leibniz Institute for Astrophysics Potsdam (AIP), and the Institute for Astronomy and Astro-

physics of the University of Tübingen, with the support of DLR and the Max Planck Society. The Argelander Institute for Astronomy of the University of Bonn and the Ludwig Maximilians Universität Munich also participated in the science preparation for *eROSITA*.

Facilities: Rubin:Simonyi (LSSTComCam), USDAC, USDF, XMM-Newton, Chandra, Swift, *eROSITA*, Gaia

Software: LSST Science Pipelines (Rubin Observatory Science Pipelines Developers 2025), Rubin Data Butler (Jenness et al. 2022), Astropy (Astropy Collaboration et al. 2013, 2018, 2022), Astroquery (Ginsburg et al. 2019), Matplotlib (Hunter 2007), NumPy (van der Walt et al. 2011; Harris et al. 2020), LSDB (Caplar et al. 2025).

REFERENCES

- Astropy Collaboration, Robitaille, T. P., Tollerud, E. J., et al. 2013, *A&A*, 558, A33, doi: [10.1051/0004-6361/201322068](https://doi.org/10.1051/0004-6361/201322068)
- Astropy Collaboration, Price-Whelan, A. M., Sipőcz, B. M., et al. 2018, *AJ*, 156, 123, doi: [10.3847/1538-3881/aabc4f](https://doi.org/10.3847/1538-3881/aabc4f)
- Astropy Collaboration, Price-Whelan, A. M., Lim, P. L., et al. 2022, *ApJ*, 935, 167, doi: [10.3847/1538-4357/ac7c74](https://doi.org/10.3847/1538-4357/ac7c74)
- Blum, R., & the Rubin Operations Team. 2020, Vera C. Rubin Observatory Data Policy, Data Management Operations Controlled Document RDO-013, Vera C. Rubin Observatory. <https://ls.st/RDO-013>
- Budavári, T., & Basu, A. 2016, *AJ*, 152, 86
- Budavári, T., & Szalay, A. S. 2008, *ApJ*, 679, 301
- Bykov, S. D., Belvedersky, M. I., & Gilfanov, M. R. 2022, *Astronomy Letters*, 48, 653, doi: [10.1134/S1063773722110044](https://doi.org/10.1134/S1063773722110044)
- Caplar, N., Beebe, W., Branton, D., et al. 2025, arXiv e-prints, arXiv:2501.02103, doi: [10.48550/arXiv.2501.02103](https://doi.org/10.48550/arXiv.2501.02103)
- Choi, Y., Olsen, K. A. G., Carlin, J. L., et al. 2025, arXiv e-prints, arXiv:2507.01343, doi: [10.48550/arXiv.2507.01343](https://doi.org/10.48550/arXiv.2507.01343)
- Drake, A. J., Gänsicke, B. T., Djorgovski, S. G., et al. 2014, *MNRAS*, 441, 1186, doi: [10.1093/mnras/stu639](https://doi.org/10.1093/mnras/stu639)
- Evans, I. N., Evans, J. D., Martínez-Galarza, J. R., et al. 2024, *ApJS*, 274, 22, doi: [10.3847/1538-4365/ad6319](https://doi.org/10.3847/1538-4365/ad6319)
- Evans, P. A., Page, K. L., Osborne, J. P., et al. 2020, *ApJS*, 247, 54, doi: [10.3847/1538-4365/ab7db9](https://doi.org/10.3847/1538-4365/ab7db9)
- Flesch, E. W. 2023, *The Open Journal of Astrophysics*, 6, 49, doi: [10.21105/astro.2308.01505](https://doi.org/10.21105/astro.2308.01505)
- Gaia Collaboration, Vallenari, A., Brown, A. G. A., et al. 2023, *A&A*, 674, A1, doi: [10.1051/0004-6361/202243940](https://doi.org/10.1051/0004-6361/202243940)
- Ginsburg, A., Sipőcz, B. M., Bresseur, C. E., et al. 2019, *AJ*, 157, 98, doi: [10.3847/1538-3881/aafc33](https://doi.org/10.3847/1538-3881/aafc33)
- Guy, L. P., Bechtol, K., Bellm, E., et al. 2025, Rubin Observatory Plans for an Early Science Program, Technical Note RTN-011, Vera C. Rubin Observatory. <https://rtn-011.lsst.io/>
- Gwyn, S. 2024, Mapping Gaia magnitudes to LSST bands, LSST Community Forum. <https://community.lsst.org/t/mapping-gaia-magnitudes-to-lsst-bands/8927/2>
- Haakonsen, C. B., & Rutledge, R. E. 2009, *ApJS*, 184, 138
- Harris, C. R., Millman, K. J., van der Walt, S. J., et al. 2020, *Nature*, 585, 357, doi: [10.1038/s41586-020-2649-2](https://doi.org/10.1038/s41586-020-2649-2)
- Hasinger, G. 2008, *A&A*, 490, 905, doi: [10.1051/0004-6361:200809839](https://doi.org/10.1051/0004-6361:200809839)
- Hunter, J. D. 2007, *Computing in Science and Engineering*, 9, 90, doi: [10.1109/MCSE.2007.55](https://doi.org/10.1109/MCSE.2007.55)
- Ivezić, Ž., Kahn, S. M., Tyson, J. A., et al. 2019, *ApJ*, 873, 111, doi: [10.3847/1538-4357/ab042c](https://doi.org/10.3847/1538-4357/ab042c)
- Jenness, T., Bosch, J. F., Salmikov, A., et al. 2022, in Society of Photo-Optical Instrumentation Engineers (SPIE) Conference Series, Vol. 12189, Software and Cyberinfrastructure for Astronomy VII, 1218911, doi: [10.1117/12.2629569](https://doi.org/10.1117/12.2629569)
- Kaiser, N. 2004, in Society of Photo-Optical Instrumentation Engineers (SPIE) Conference Series, Vol. 5489, Ground-based Telescopes, ed. J. M. Oschmann, Jr., 11–22, doi: [10.1117/12.552472](https://doi.org/10.1117/12.552472)
- Kato, T., Isogai, K., Hamsch, F.-J., et al. 2017, *PASJ*, 69, 75, doi: [10.1093/pasj/psx058](https://doi.org/10.1093/pasj/psx058)
- Luo, B., Brandt, W. N., Xue, Y. Q., et al. 2017, *ApJS*, 228, 2, doi: [10.3847/1538-4365/228/1/2](https://doi.org/10.3847/1538-4365/228/1/2)
- Malanchev, K., DeLucchi, M., Caplar, N., et al. 2025, arXiv e-prints, arXiv:2506.23955, doi: [10.48550/arXiv.2506.23955](https://doi.org/10.48550/arXiv.2506.23955)
- Merloni, A., Lamer, G., Liu, T., et al. 2024, *A&A*, 682, A34, doi: [10.1051/0004-6361/202347165](https://doi.org/10.1051/0004-6361/202347165)

- NSF-DOE Vera C. Rubin Observatory. 2025a, The Vera C. Rubin Observatory Data Preview 1, doi: [10.71929/rubin/2570536](https://doi.org/10.71929/rubin/2570536)
- . 2025b, Legacy Survey of Space and Time Data Preview 1: object dataset type [Data set], NSF-DOE Vera C. Rubin Observatory, doi: [10.71929/RUBIN/2570324](https://doi.org/10.71929/RUBIN/2570324)
- . 2025c, Legacy Survey of Space and Time Data Preview 1: deep_coadd dataset type, NSF-DOE Vera C. Rubin Observatory, doi: [10.71929/RUBIN/2570313](https://doi.org/10.71929/RUBIN/2570313)
- . 2025d, Legacy Survey of Space and Time Data Preview 1: visit_image dataset type [Data set], NSF-DOE Vera C. Rubin Observatory, doi: [10.71929/RUBIN/2570311](https://doi.org/10.71929/RUBIN/2570311)
- . 2025e, Legacy Survey of Space and Time Data Preview 1: object_forced_source dataset type [Data set], NSF-DOE Vera C. Rubin Observatory, doi: [10.71929/RUBIN/2570326](https://doi.org/10.71929/RUBIN/2570326)
- . 2025f, Legacy Survey of Space and Time Data Preview 1: difference_image dataset type [Data set], NSF-DOE Vera C. Rubin Observatory, doi: [10.71929/RUBIN/2570312](https://doi.org/10.71929/RUBIN/2570312)
- . 2025g, Legacy Survey of Space and Time Data Preview 1: dia_source dataset type [Data set], NSF-DOE Vera C. Rubin Observatory, doi: [10.71929/RUBIN/2570316](https://doi.org/10.71929/RUBIN/2570316)
- . 2025h, Legacy Survey of Space and Time Data Preview 1: dia_object dataset type [Data set], NSF-DOE Vera C. Rubin Observatory, doi: [10.71929/RUBIN/2570318](https://doi.org/10.71929/RUBIN/2570318)
- . 2025i, Legacy Survey of Space and Time Data Preview 1: dia_object_forced_source dataset type [Data set], NSF-DOE Vera C. Rubin Observatory, doi: [10.71929/RUBIN/2570320](https://doi.org/10.71929/RUBIN/2570320)
- Richter, G. A. 1975, *Astronomische Nachrichten*, 296, 65, doi: [10.1002/asna.19752960203](https://doi.org/10.1002/asna.19752960203)
- Rodriguez, A. C. 2024, *PASP*, 136, 054201, doi: [10.1088/1538-3873/ad357c](https://doi.org/10.1088/1538-3873/ad357c)
- Rubin Observatory Science Pipelines Developers. 2025, The LSST Science Pipelines Software: Optical Survey Pipeline Reduction and Analysis Environment, Project Science Technical Note PSTN-019, Vera C. Rubin Observatory, doi: [10.71929/rubin/2570545](https://doi.org/10.71929/rubin/2570545)
- Rutledge, R. E., Brunner, R. J., Prince, T. A., & Lonsdale, C. 2000, *ApJS*, 131, 335
- Salvato, M., Buchner, J., Budavári, T., et al. 2018, *MNRAS*, 473, 4937, doi: [10.1093/mnras/stx2651](https://doi.org/10.1093/mnras/stx2651)
- Saxton, R. D., Read, A. M., Esquej, P., et al. 2008, *A&A*, 480, 611, doi: [10.1051/0004-6361:20079193](https://doi.org/10.1051/0004-6361:20079193)
- Shi, X., Budavári, T., & Basu, A. 2019, *ApJ*, 870, 51
- Stetson, P. B. 1996, *PASP*, 108, 851, doi: [10.1086/133808](https://doi.org/10.1086/133808)
- Sutherland, W., & Saunders, W. 1992a, *MNRAS*, 259, 413, doi: [10.1093/mnras/259.3.413](https://doi.org/10.1093/mnras/259.3.413)
- . 1992b, *MNRAS*, 259, 413, doi: [10.1093/mnras/259.3.413](https://doi.org/10.1093/mnras/259.3.413)
- van der Walt, S., Colbert, S. C., & Varoquaux, G. 2011, *Computing in Science and Engineering*, 13, 22, doi: [10.1109/MCSE.2011.37](https://doi.org/10.1109/MCSE.2011.37)
- Wainer, T. M., Davenport, J. R. A., Bellm, E. C., et al. 2025, arXiv e-prints, arXiv:2507.03228, doi: [10.48550/arXiv.2507.03228](https://doi.org/10.48550/arXiv.2507.03228)
- Webb, N. A., Coriat, M., Traulsen, I., et al. 2020, *A&A*, 641, A136, doi: [10.1051/0004-6361/201937353](https://doi.org/10.1051/0004-6361/201937353)
- Wenger, M., Ochsenbein, F., Egret, D., et al. 2000, *A&AS*, 143, 9, doi: [10.1051/aas:2000332](https://doi.org/10.1051/aas:2000332)
- Wevers, T., Hodgkin, S. T., Jonker, P. G., et al. 2016, *MNRAS*, 458, 4530, doi: [10.1093/mnras/stw643](https://doi.org/10.1093/mnras/stw643)
- York, D. G., Adelman, J., Anderson, Jr., J. E., et al. 2000, *AJ*, 120, 1579, doi: [10.1086/301513](https://doi.org/10.1086/301513)